

Mechanical Performance and Internal Porosity of 3D Printed PLA Across Varying Parameters

Roman Chavez^a, Nathan Nevarez^a, Fidel Baez Avila^a, Borys Drach^a

^a Department of Mechanical and Aerospace Engineering, New Mexico State University,
Las Cruces, NM 88003

Abstract

This study investigates the impact of layer height (LH) and line width (LW) on the porosity and mechanical performance of polylactic acid (PLA) fabricated via fused filament fabrication using a Bambu Lab P1S 3D printer. Cylindrical specimens with 8-mm diameter were manufactured, then imaged via X-ray computed tomography to analyze porosity at different LH and LW mixtures. Dog bone specimens were manufactured in accordance with ASTM D638 in both horizontal and vertical orientations and subjected to uniaxial tensile testing. Yield strength (YS) and ductility are significantly more sensitive to the examined printing parameters compared to Young's modulus. There is a positive correlation between YS and LW in the case of vertical orientation of the dog bone specimens, and negative in the case of horizontal. No clear dependence of mechanical properties on pore volume fraction was observed in our study. Pore network morphologies are presented for each combination of parameters.

Introduction

Fused filament fabrication (FFF) is an additive manufacturing technique (AM) that uses a filament type thermoplastic which is fed through a heated nozzle, where it is partially melted, and then deposited layer by layer [1]. FFF has become increasingly popular in polymer-based 3D printing due to its affordability, accessibility, and rapid prototyping capabilities [1–3]. This process allows for the creation of complex geometries that would be difficult or impossible to achieve through traditional manufacturing methods [1]. Among the many material options available for FFF, PLA is the most widely used filament due to its affordability, ease of use, and low printing temperature [1–3].

There is a significant amount of literature studying the many printing parameters that can be controlled to manipulate mechanical performance for a given function of a part. Printing parameters include but are not limited to: layer height, line width, printing speed, nozzle temperature, nozzle diameter, and build orientation [1–6]. Build orientation refers to how the sample is printed on the build plate, lying flat horizontally or standing upright. Build orientation has a significant impact on mechanical properties, in particular ductility and failure behavior [3,6–9]. Conclusions about layer height's (LH) effect on mechanical properties vary. In many publications [3,8,9], it was found that LH has a significant impact on tensile performance. Results from Tymrak et al. [10] contradict these findings by illustrating layer height in horizontally printed specimens plays no significant contribution on mechanical performance. In Chacon et al. [3], layer

height displayed slight significance in mechanical performance in horizontal builds. These specimens benefited by having lower layer heights, resulting in higher tensile strength and a decrease in flexural strength [3]. Many publications concluded that increased layer heights within vertical build orientations maximizes mechanical performance, citing better homogeneity of “beads” (deposited filament) [3,6,8,11]. One of the more underreported parameters is the line width, specifically its effect on porosity and mechanical performance.

X-ray computed tomography (CT) has been increasingly utilized for non-destructive evaluation of additive manufactured parts, enabling a detailed reconstruction of internal structures. CT works by capturing thousands of X-ray projections of a specimen, each one from a slightly different angle, until the specimen completes one rotation [12]. A three-dimensional model is reconstructed from the captured projections by software. This technique establishes a non-destructive internal imaging of the specimen, which allows quantification of porosity without damaging the specimen [13]. In non-destructive studies of FFF porosity has been defined as internal voids that are developed from numerous factors; the most common being from the lack of material fusion between beads [5].

In this study, various combinations of the layer height and line width parameters were chosen based on the 3D printer manufacturers’ recommendations. Cylindrical specimens for all layer height/line width combinations were fabricated via FFF for porosity analysis via CT. Dog bone specimens were then manufactured for uniaxial tensile testing in two build orientations. Tensile mechanical properties of the dog bone specimens were compared to internal porosity found within cylinders. This study investigates correlations between porosity, mechanical performance, and print parameters.

Materials and Methods

3D Printed Specimens

All cylindrical and dog-bone (DB) specimens were fabricated via a Bambu Lab (Shenzhen, China) P1S FFF 3D printer using a standard 0.4mm nozzle and Bambu Lab’s Jada White PLA basic filament with a diameter of 1.75 mm. White filament was selected to eliminate the dimensional variation often associated with additives in colored filament [14]. Before every print, the PLA filament was dried at 52°C for 8 hours in a blast drying oven as recommended by the manufacturer to prevent potential printing inconsistencies due to the filament absorbing moisture. Defaults set by the Bambu Lab slicer software for the P1S printer and PLA filament were used for most parameters to manufacture all specimens including but not limited to a flow ratio of 0.98, nozzle temperature of 220°C, and a bed temperature of 55°C. Default value of 15% infill was changed to 100% (+45°/-45° hatch pattern) in order to create fully dense specimens. All specimens were printed on a high temperature smooth PEI plate.

Two print parameters, layer height (LH) and line width (LW) were varied between the prints. Parameter sets were developed by combining each LH value (0.08mm, 0.20mm, and 0.28mm) with each LW value (0.31mm, 0.42mm, and 0.62mm), creating 9 different mixtures. Selected LH values span the full range of the values enabled by the Bambu Lab’s slicer software for the 0.4mm nozzle on the P1S 3D printer. The selected values for the LW parameter represent a portion of the full range available in the software (0.2mm – 1mm) and are based on the printer manufacturer’s recommendation to keep line width between 75% and 150% of the nozzle diameter [15]. Bambu Lab’s default parameters 0.20mm LH/0.42mm LW were used as a benchmark. The

9 parameter combinations along with their reference IDs are provided in Table 1 for horizontal and vertical dog bone specimens.

Table 1. Print parameter combinations and their reference IDs.

#	Line Width	Layer Height	Horizontal Orientation IDs	Vertical Orientation IDs
1	0.31mm	0.08mm	DB1A	DB1D
2	0.31mm	0.20mm	DB1B	DB1E
3	0.31mm	0.28mm	DB1C	DB1F
4	0.42mm	0.08mm	DB2A	DB2D
5	0.42mm	0.20mm	DB2B	DB2E
6	0.42mm	0.28mm	DB2C	DB2F
7	0.62mm	0.08mm	DB3A	DB3D
8	0.62mm	0.20mm	DB3B	DB3E
9	0.62mm	0.28mm	DB3C	DB3F

Cylindrical specimens used for porosity analysis via CT had a diameter of 8 mm and a height of 12 mm. One cylindrical specimen was manufactured in a vertical print orientation for each mixture group shown in Table 1, resulting in nine specimens. See Figure 1 for illustration of reconstructed external surfaces of three of those specimens. Dog bone specimens were manufactured in accordance with ASTM D638 standard [16] (type 1 specimen). Each dog bone had a thickness of 6mm and was printed with one wall loop. Five dog bone specimen replicates were manufactured for each combination in Table 1 in both horizontal and vertical orientations resulting in a total of 90 specimens. While the cylindrical specimens were only manufactured in the vertical orientation, it is important to point out that CT results in full volumetric imaging of the internal porosity which enables analysis of pore distribution in longitudinal and transverse directions in each specimen regardless of printing orientation.

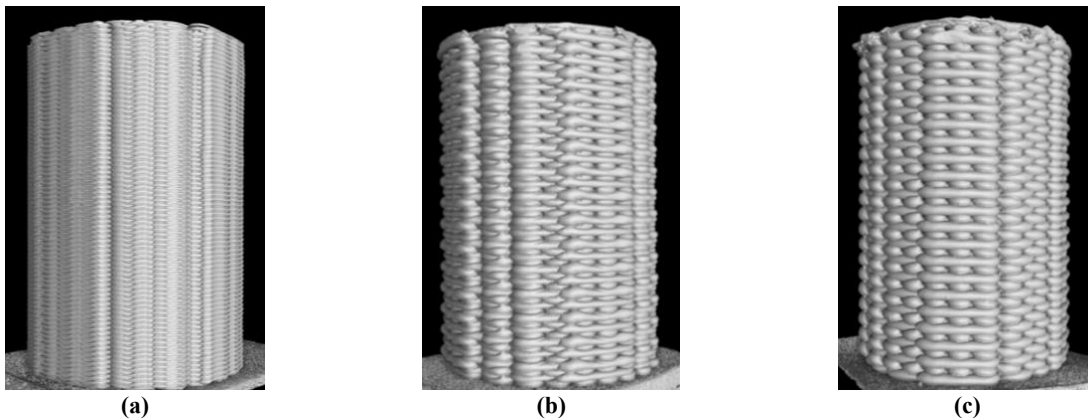


Figure 1. External surfaces of the 8 mm × 12 mm cylindrical specimens used for porosity analysis reconstructed from CT data: (a) 0.42 mm LW × 0.08 mm LH, (b) 0.42 mm LW × 0.20 mm LH, and (c) 0.42 mm LW × 0.28 mm LH.

Tensile Testing

Uniaxial tensile testing of dog bone specimens was conducted on an Instron 6800 series Universal Testing Machine following the ASTM D638 guidelines, see Figure 2 for the experimental setup. Specimens were loaded at a crosshead speed of 5 mm/min, with a 2-inch clip-on extensometer used for capturing strain. Prior to tensile testing, dimensions of each specimen were measured: overall length, average thickness, and average test section width. Actual as opposed to nominal dimensions, were used for engineering stress calculations.

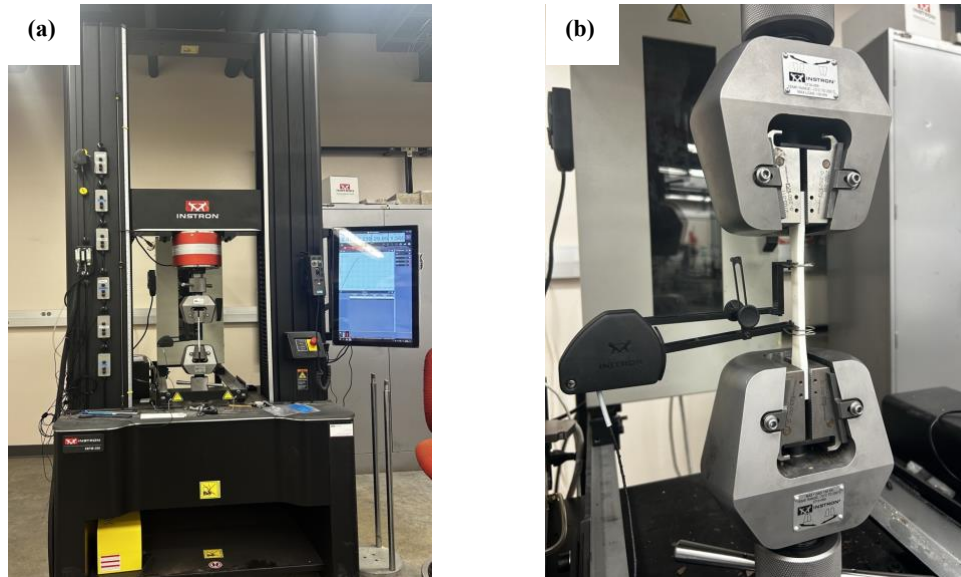


Figure 2. Tensile testing experimental setup (a) general view, and (b) close-up view showing the positioning of the extensometer.

X-Ray Computed Tomography

Computed tomography (CT) imaging was acquired using Waygate Technologies Phoenix V|tome|xS dual micro/nano tube CT scanner. Cylindrical specimens used for porosity analyses were scanned using the nano tube with the following parameters: voltage of 45kV, current of 650 μ A, sensitivity of 1, and a voxel size of 13.1 μ m. Scans were reconstructed via Waygate Datos X and transverse slice TIFF image stacks containing 1500 projections each were exported via VG Studio Max for further processing in ORS Dragonfly. In ORS Dragonfly, reconstructed porosity was cropped to a region of interest measuring 4.8 mm \times 4.8 mm \times 10.7 mm, see Figure 3. This cropping removed areas with overlapping “beads” (deposited filament lines) at the cylinder’s circumference, which were generated when the printhead reversed direction during printing resulting in reduced porosity compared to the rest of the specimen. Prior to cropping, Otsu’s thresholding method implemented in ORS Dragonfly was used to separate pores from the bulk PLA material. Otsu’s

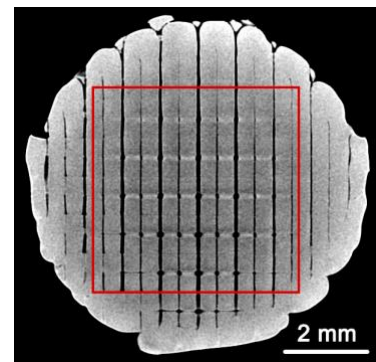


Figure 3. Region of interest for porosity analysis of a cylindrical specimen.

method computes a single intensity value that represents a threshold between foreground and background classes by minimizing the intra-class variation. Finally, pores smaller than 9 voxels by volume were removed.

Mechanical Property Computation

Force and engineering strain data were recorded by the Instron Bluehill software during tensile testing of dog bone specimens. The data was processed using a custom Matlab script to calculate engineering stress, Young’s modulus, yield strength, elongation at break, and plot stress-strain curves for each test.

Strength (yield strength for horizontal, and ultimate tensile strength for vertical specimens) was computed by locating the yield point in the case of a ductile specimen or maximum stress in the case of a brittle specimen. Two different functions were used to determine the elongation at break. The first one relies on the strain value corresponding to a sudden drop in stress during testing; it was used for specimens with a clear abrupt fracture. The second function extracts the strain at which stress first drops to zero; it was used for specimens exhibiting ductile response.

Results from specimens that broke outside of the extensometer gauge length or near its blades were not used for calculations. When this occurred, additional specimens were fabricated and tested.

Results and Discussion

Porosity Analysis

CT imaging acquired on cylindrical specimens was used to examine the relationship between pore volume fraction, pore morphology, and mechanical performance of the 3D printed dog bone specimens. Table 2 presents the pore volume fractions for each combination of the layer height and line width print parameters.

Table 2. Pore volume fraction for each LW and LH parameter combination.

		Line Width		
		0.31mm	0.42mm	0.62mm
Line Height	0.08mm	0.01%	0.52%	0.02%
	0.20mm	1.61%	0.65%	0.59%
	0.28mm	0.75%	0.40%	0.51%

Figure 4 presents a visualization of porosity for each of the 9 cylinders printed using the parameter combinations detailed in Table 1. Each sub-figure contains two images – top and side views of the corresponding cylinder. Color corresponds to the volume of a pore with warmer colors representing greater volume. Caution is advised when interpreting pore volume distributions due to the nature of the porosity in this case – pore network is comprised of long thin “tunnels”.

Continuity of these tunnels and therefore volume of a single connected pore are highly sensitive to thresholding and would be affected substantially in response to a small change in the threshold value. Nevertheless, there appears to be a spatial dependence of the connected pore volume for some combinations with the most pronounced effect in the cases of 0.42mm LW x 0.28mm and 0.62 LW x 0.28 LH – pores appear to be more interconnected near the build plate.

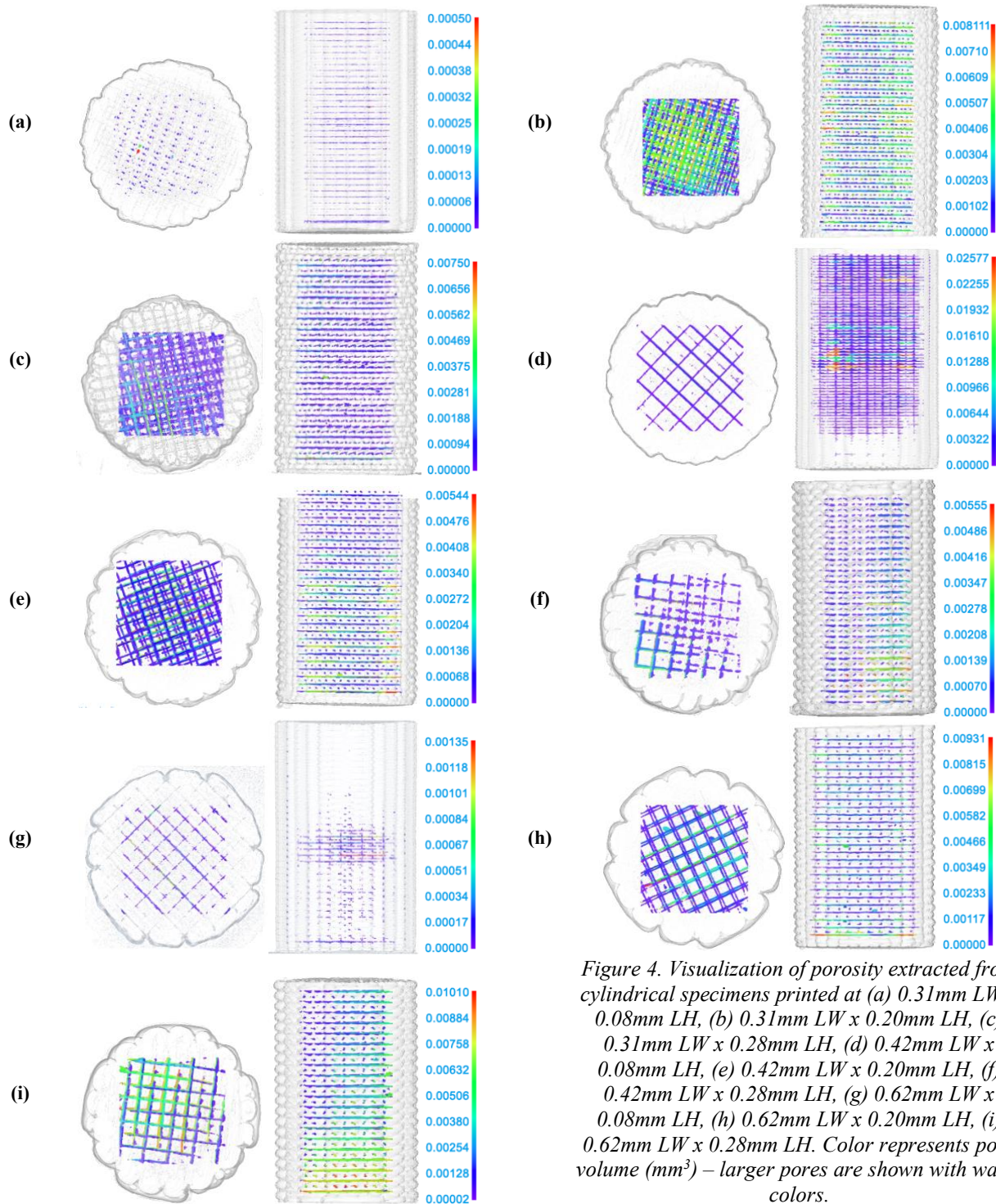


Figure 4. Visualization of porosity extracted from cylindrical specimens printed at (a) 0.31mm LW x 0.08mm LH, (b) 0.31mm LW x 0.20mm LH, (c) 0.31mm LW x 0.28mm LH, (d) 0.42mm LW x 0.08mm LH, (e) 0.42mm LW x 0.20mm LH, (f) 0.42mm LW x 0.28mm LH, (g) 0.62mm LW x 0.08mm LH, (h) 0.62mm LW x 0.20mm LH, (i) 0.62mm LW x 0.28mm LH. Color represents pore volume (mm^3) – larger pores are shown with warm colors.

Differences in the overall volume and spacing between pore tunnels are clearly visible in these figures. From examination of the side views, vertical spacing between the tunnels is a function of LH – greater LH values result in larger spacing. In-plane spacing can be seen in the top views. Greater LW values are expected lead to larger in-plane spacing; however, apparent spacing does not seem to follow this trend. The largest apparent in-plane spacing is seen in the case of intermediate value of layer width – 0.42mm LW x 0.08mm LH combination (Figure 4d). Upon closer examination, it appears that every other tunnel is very faint which gives an impression of much larger in-plane spacing. Another effect making interpretation of pore tunnel spacing in the top views challenging is vertical alignment of the tunnels between every other layer. For example, pore tunnels in all three 0.08mm LH cylinders (Figure 4a, Figure 4d, and Figure 4g) are close to perfectly aligned as seen in side views. Other combinations exhibit varying degrees of misalignment giving an impression of much higher apparent density in the top views. Combinations with the lowest measured pore volume fractions (see Table 2), i.e. 0.31mm LW x 0.08mm LH (Figure 4a) and 0.62mm LW x 0.08mm LH (Figure 4g) are easily identifiable in these images.

The pore “tunnels” are formed above the interface between adjacent parallel beads, resulting from unfilled spaces due to the rounded geometry of the bead cross-sections, see Figure 5. There are virtually no pores inside the beads. The number of the pore tunnels is a function of the print parameters – increasing line width results in fewer beads in a transverse plane which leads to fewer pore tunnels in the plane. Increasing layer height results in thicker beads and fewer of them across the height of the cylinder leading to fewer pore tunnels along the longitudinal direction.

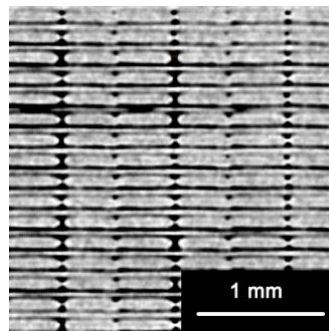


Figure 5. Longitudinal cross-section of a cylindrical specimen (0.08 mm LH x 0.42 mm LW) illustrating pore morphology in 3D printed specimens considered in this study. Light areas: beads, black areas: pores.

Mechanical Properties

Stress-strain plots from tensile testing of 3D printed dog bone specimens are shown Figure 6. The sub-figures are organized in a 3×2 grid: each column presents results for a different build orientation (horizontal or vertical), and each row corresponds to a different line width (0.31 mm, 0.42 mm, and 0.62 mm). Each sub-figure contains representative stress-strain plots for three values of layer height (0.08 mm, 0.20 mm, and 0.28 mm). Numerical values for Young’s modulus, strength, and elongation at break are summarized in Table 3 and also illustrated via bar charts in Figure 7.

Young’s modulus appears to be the least impacted property among the three examined to changes in LH and LW print parameters or build orientation. The maximum value of 2409.2 MPa (averaged over 5 replicates) was obtained in the case of the horizontal orientation at 0.08 mm LH × 0.31 mm LW, while the minimum value of 2127.2 MPa was also measured in the case of horizontal orientation at 0.28 mm LH × 0.42 mm LW. No trend could be identified for Young’s modulus with respect to LH, LW, or their interaction.

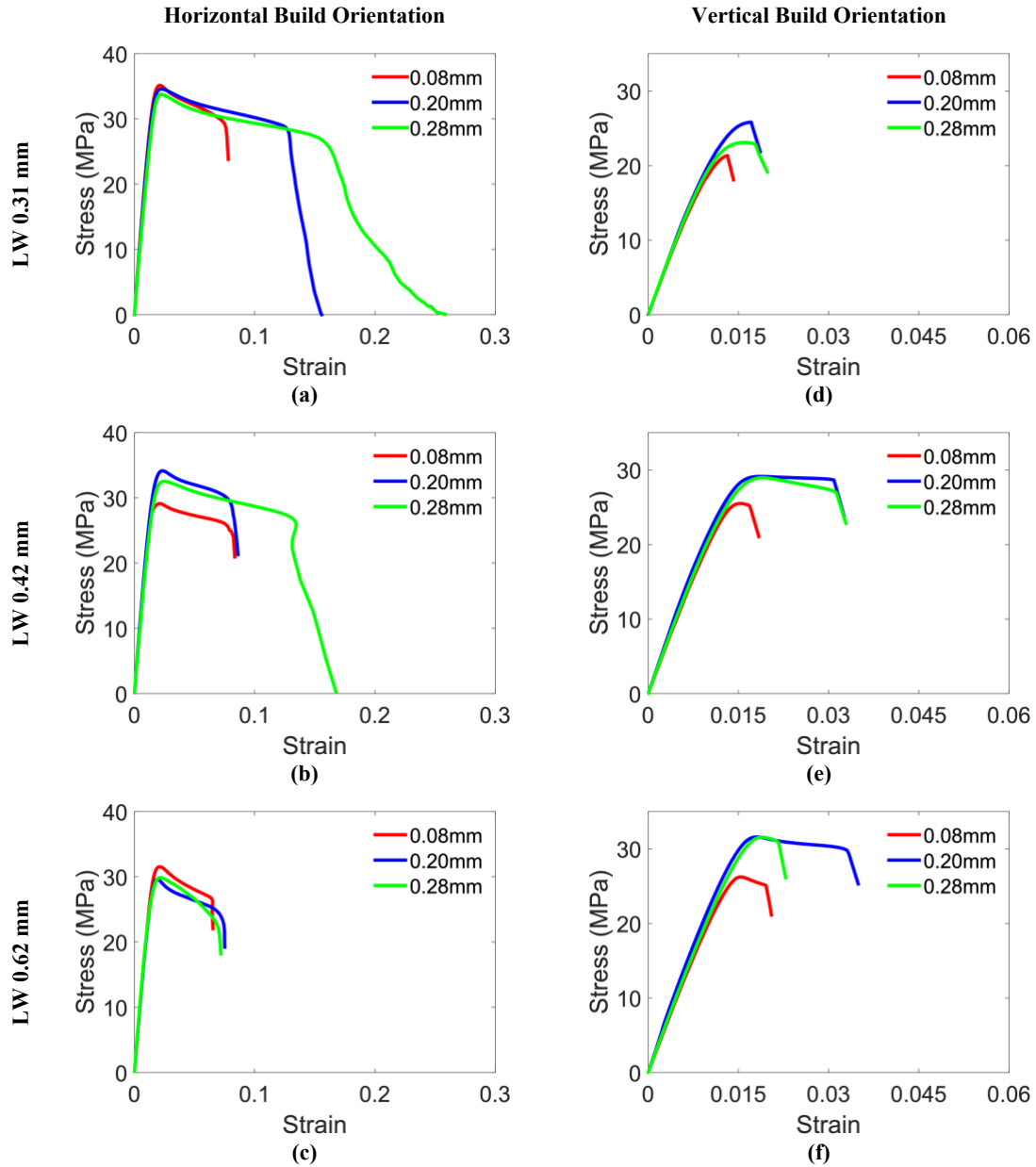


Figure 6. Stress–strain curves from tensile tests of dog bone specimens printed with different combinations of LW, LH, and build orientation.

All horizontal specimens underwent ductile failure (elongation at break $\epsilon_b > 6.47\%$ with a mean value of 11.57%) while all vertical specimens failed in a rather brittle manner ($\epsilon_b < 4.04\%$ with a mean value of 2.46%). The significantly lower ductility and strength of the vertically oriented specimens point to the weak nature of the interface between layers. In addition to build orientation, line width as well as layer height appear to affect ductility. There is a positive correlation between LH and ϵ_b for both orientations. Lower ductility in vertical specimen at lower values of LH can be explained by a large number of weak and seemingly brittle layer interfaces – these interfaces are pulled apart during tensile testing of vertical specimens. The reason for brittleness of horizontally printed specimens at 0.08 mm LH is not immediately obvious. One potential explanation may be seen in Figure 5 – beads appear severely compressed due to the small

distance between layers. As a result, there are large gaps between adjacent beads of the same layer in some locations leading to poor performance. While a low LH enhances the dimensional accuracy of small features, it compromises the material's strength and ductility.

Elongation at break ϵ_b is sensitive to changes in LW – it decreases with increasing LW in the case of horizontal specimens and increases slightly in the case of vertical build orientation. The maximum and minimum values of ϵ_b for horizontal specimens are 26.15% (0.28 mm LH \times 0.31 mm LW) and 6.47% (0.08 mm LH \times 0.62 mm LW), correspondingly. For the vertical specimens, these values are 4.04% (0.20 mm LH \times 0.62 mm LW) and 1.43% (0.08 mm LH \times 0.31 mm LW).

Yield strength in horizontal specimens and ultimate tensile strength in vertical specimens appear to depend primarily on line width, with horizontal specimens showing greater strength at thinner line widths, and vertical specimens at thicker ones. Horizontal specimen yield strength decreased from 34.34 MPa at 0.31 mm LW (averaged over LH values) to 30.37 MPa at 0.62 mm LW. On the other hand, ultimate strength increased from 23.49 MPa at 0.31 mm LW to 29.86 MPa at 0.62 mm LW in the case of vertically printed specimens. These trends partially resemble those observed earlier for elongation at break.

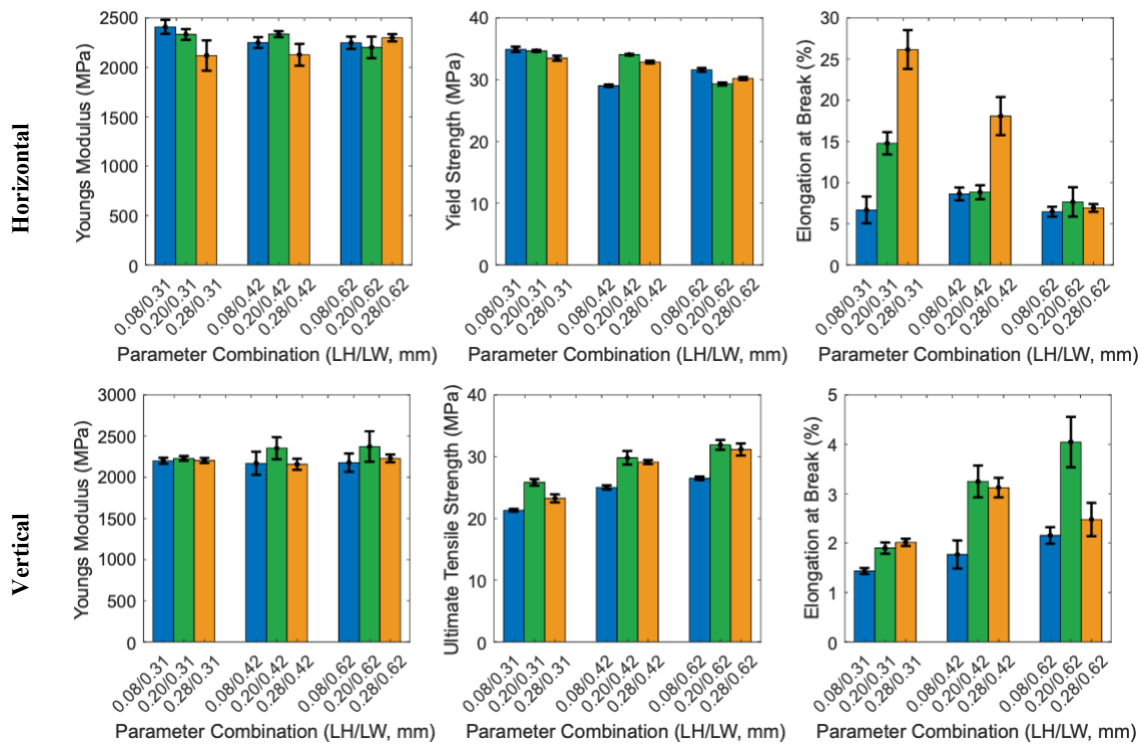


Figure 7. Bar charts showing Young's modulus, strength, and elongation at break for different combinations of LW, LH, and build orientation.

Comparing these trends in mechanical properties to pore volume fractions presented in Table 2 does not yield any immediate correlation. For example, the combination with lowest porosity value (0.08 mm LH \times 0.31 mm LW) consistently performed the worst in terms of ductility

among all parameter combinations in both horizontal and vertical sets. Vertically oriented specimens printed at 0.08 mm LH had the lowest ultimate tensile strength for all LW values. These observations combined with objectively low porosity observed in all specimens point to the importance of the number and quality of layer-to-layer and bead-to-bead interfaces for mechanical performance of 3D printed PLA specimens rather than total volumetric porosity. Some preliminary observations can be made based on the presented results. For example, interlayer adhesion appears to improve with increased volumetric flow – both strength and ductility of vertically oriented specimens increase with increased LW and LH parameters. We performed preliminary optical and scanning electron microscopy of polished PLA samples in an attempt to observe differences between interfaces obtained from different printing parameters. However, no structural differences were immediately apparent. Further investigations into the amount of crystallinity and the degree of molecular chain entanglement at layer and bead interfaces, across different LH and LW values, could help clarify how these print parameters influence strength and ductility.

Table 3. Summary of Young’s modulus, strength, and elongation at break for different combinations of LH, LW, and build orientation. Values represent the mean of five replicates per combination, with standard deviations shown in square brackets.

Horizontal Specimens									
	Young’s Modulus, MPa			Yield Strength, MPa			Elongation at Break, %		
LH/LW	0.31mm	0.42mm	0.62mm	0.31mm	0.42mm	0.62mm	0.31mm	0.42mm	0.62mm
0.08mm	2409.17 [70.82]	2250.61 [55.25]	2248.70 [61.31]	34.91 [0.42]	29.01 [0.21]	31.59 [0.31]	6.68 [1.63]	8.63 [0.77]	6.47 [0.59]
0.20mm	2333.17 [54.63]	2336.29 [29.70]	2201.81 [108.2]	34.65 [0.18]	34.05 [0.11]	29.31 [0.25]	14.77 [1.35]	8.83 [0.86]	7.65 [1.79]
0.28mm	2119.32 [153.08]	2127.16 [111.10]	2299.45 [36.72]	33.48 [0.39]	32.84 [0.22]	30.20 [0.25]	26.15 [2.36]	18.07 [2.31]	6.92 [0.47]

Vertical Specimens									
	Young’s Modulus, MPa			Ultimate Strength, MPa			Elongation at Break, %		
LH/LW	0.31mm	0.42mm	0.62mm	0.31mm	0.42mm	0.62mm	0.31mm	0.42mm	0.62mm
0.08mm	2199.59 [36.30]	2168.88 [139.90]	2177.66 [110.10]	21.36 [0.22]	25.02 [0.36]	26.50 [0.30]	1.43 [0.06]	1.77 [0.29]	2.15 [0.17]
0.20mm	2229.48 [28.90]	2353.59 [134.0]	2373.34 [184.90]	25.85 [0.52]	29.83 [1.08]	31.92 [0.79]	1.90 [0.11]	3.25 [0.32]	4.04 [0.51]
0.28mm	2204.04 [31.60]	2158.09 [68.30]	2229.15 [46.30]	23.26 [0.66]	29.12 [0.32]	31.17 [0.97]	2.01 [0.07]	3.12 [0.20]	2.47 [0.34]

Conclusions

This study investigated the effects varying printing parameters – line width, layer height, and build orientation – have on Young’s modulus, strength, and ductility of FFF printed PLA specimens. Our initial hypothesis was that the mechanical properties would strongly correlate with

specimen pore volume fraction which would be a function of printing parameters. CT imaging was used to perform a detailed porosity analysis in an initial effort to connect porosity with printing parameters and mechanical properties of the PLA specimens. It was indeed observed that porosity morphology varied significantly throughout the different parameter combinations. However, there were no definitive trends that allowed for a correlation to be drawn between the porosity percentage and mechanical performance. Instead, it is inferred, that mechanical performance is a function of interface properties, such as the number and quality of layer and bead interfaces. On the other hand, there are clear trends in strength and ductility of specimens printed at different line width, layer height, and build orientation.

Out of the three parameters considered (Young's modulus, strength, and ductility), Young's modulus appears to be the least affected by print parameters or build orientation. As expected vertically printed specimens exhibited lower strength and significantly reduced ductility compared to the horizontally printed specimens. Results showed that correlation between strength and line width was negative in the case of horizontal build orientation and positive in the case of vertical build orientation. Layer height had a significant impact on strength in the case of vertical build orientation – 0.08 mm resulted in the lowest strength across all considered line width values. This finding is in line with existing research. On the other hand, there was no clear trend in strength values in response to changes in layer height in the case of horizontal specimens contradicting some of the previous studies. Ductility appears to be a function of both line width and layer height with the most dramatic difference observed in the case of horizontal specimens printed at 0.31 mm LW – average elongation at break increased from 6.68% at 0.08 mm LH to 26.15% at 0.28 mm LH.

Our research supports the choice of the layer height of 0.20 mm and line width of 0.42 mm for 0.4-mm nozzles already used as default settings by most slicer software packages in consumer 3D printing. This combination results in a balanced trade-off between strength and ductility for 3D-printed parts loaded either parallel or perpendicular to the build direction. The results presented here may help advanced users optimize mechanical properties in one loading direction, while accepting reduced performance in the other. Finally, printing times should be mentioned as well. Layer height and build orientation are the primary factors affecting the total print duration. One dog bone specimen in horizontal orientation can be printed in as little as 22 minutes (0.28 mm LH × 0.62 mm LW) or in as long as 1 hour 11 minutes (0.08 mm LH × 0.31 mm LW). Printing dog bone specimens in the vertical orientation takes even longer – 50 minutes (0.28 mm LH × 0.62 mm LW) and 2 hours 56 minutes (0.08 mm LH × 0.31 mm LW), correspondingly.

Future work may focus on exploring relevance of discussed mechanical property and porosity observations to other commonly used materials (e.g. Acrylonitrile Butadiene Styrene, ABS, or Polyethylene Terephthalate Glycol, PETG), specimen geometries, and loading regimes (e.g. four-point bending, cyclic testing etc.).

Acknowledgements

This research is based on the work supported by the U.S. Department of Energy through the Minority Serving Institution Partnership Program (MSIPP) under the Grant No. DE-NA0003987 (acknowledged by the authors RC, NN, and BD), by the National Aeronautics and

Space Administration under the NASA Cooperative Agreement No. NM-80NSSC20M0215 (acknowledged by the authors RC, FBA, and BD), and by the Army Research Office under the grant No. W911NF2110138.

References

- [1] Rouf, S., Malik, A., Singh, N., Raina, A., Naveed, N., Siddiqui, M. I. H., and Haq, M. I. U., 2022, “Additive Manufacturing Technologies: Industrial and Medical Applications,” *Sustain. Oper. Comput.*, **3**, pp. 258–274. <https://doi.org/10.1016/j.susoc.2022.05.001>.
- [2] Patel, R., Desai, C., Kushwah, S., and Mangrola, M. H., 2022, “A Review Article on FDM Process Parameters in 3D Printing for Composite Materials,” *Mater. Today Proc.*, **60**, pp. 2162–2166. <https://doi.org/10.1016/j.matpr.2022.02.385>.
- [3] Chacón, J. M., Caminero, M. A., García-Plaza, E., and Núñez, P. J., 2017, “Additive Manufacturing of PLA Structures Using Fused Deposition Modelling: Effect of Process Parameters on Mechanical Properties and Their Optimal Selection,” *Mater. Des.*, **124**, pp. 143–157. <https://doi.org/10.1016/j.matdes.2017.03.065>.
- [4] Al-Maharma, A., Patil, S., and Markert, B., “Effects of Porosity on the Mechanical Properties of Additively Manufactured Components: A Critical Review,” *Mater. Research Express*, **7**(2020).
- [5] Faizaan, M., Shenoy Baloor, S., Nunna, S., Mallya, R., Rao Udipi, S., Ramanath Kini, C., Kada, S. R., and Creighton, C., 2025, “A Study on the Overall Variance and Void Architecture on MEX-PLA Tensile Properties through Printing Parameter Optimization,” *Sci. Rep.*, **15**(1), p. 3103. <https://doi.org/10.1038/s41598-025-87348-2>.
- [6] Rodríguez-Panes, A., Claver, J., and Camacho, A. M., 2018, “The Influence of Manufacturing Parameters on the Mechanical Behaviour of PLA and ABS Pieces Manufactured by FDM: A Comparative Analysis,” *Materials*, **11**(8), p. 1333. <https://doi.org/10.3390/ma11081333>.
- [7] Marşavina, L., Vălean, C., Mărghitaş, M., Linul, E., Razavi, N., Berto, F., and Brighenti, R., 2022, “Effect of the Manufacturing Parameters on the Tensile and Fracture Properties of FDM 3D-Printed PLA Specimens,” *Eng. Fract. Mech.*, **274**, p. 108766. <https://doi.org/10.1016/j.engfracmech.2022.108766>.
- [8] Zhao, Y., Chen, Y., and Zhou, Y., 2019, “Novel Mechanical Models of Tensile Strength and Elastic Property of FDM AM PLA Materials: Experimental and Theoretical Analyses,” *Mater. Des.*, **181**, p. 108089. <https://doi.org/10.1016/j.matdes.2019.108089>.
- [9] Alafaghani, A., Qattawi, A., Alrawi, B., and Guzman, A., 2017, “Experimental Optimization of Fused Deposition Modelling Processing Parameters: A Design-for-Manufacturing Approach,” *Procedia Manuf.*, **10**, pp. 791–803. <https://doi.org/10.1016/j.promfg.2017.07.079>.
- [10] Tymrak, B. M., Kreiger, M., and Pearce, J. M., 2014, “Mechanical Properties of Components Fabricated with Open-Source 3-D Printers under Realistic Environmental Conditions,” *Mater. Des.*, **58**, pp. 242–246. <https://doi.org/10.1016/j.matdes.2014.02.038>.
- [11] Sandanamsamy, L., Mogan, J., Rajan, K., Harun, W. S. W., Ishak, I., Romlay, F. R. M., Samykano, M., and Kadirgama, K., 2024, “Effect of Process Parameter on Tensile Properties of FDM Printed PLA,” *Mater. Today Proc.*, **109**, pp. 1–6. <https://doi.org/10.1016/j.matpr.2023.03.217>.

- [12] Townsend, A., Senin, N., Blunt, L., Leach, R. K., and Taylor, J. S., 2016, "Surface Texture Metrology for Metal Additive Manufacturing: A Review," *Precis. Eng.*, **46**, pp. 34–47. <https://doi.org/10.1016/j.precisioneng.2016.06.001>.
- [13] Thompson, A., Maskery, I., and Leach, R., 2016, "X-Ray Computed Tomography for Additive Manufacturing: A Review," *Meas. Sci. Technol.*, **27**(072001). <https://doi.org/10.1088/0957-0233/27/7/072001>.
- [14] Frunzaverde, D., Cojocaru, V., Bacescu, N., Ciubotariu, C.-R., Miclosina, C.-O., Turiac, R. R., and Marginean, G., 2023, "The Influence of the Layer Height and the Filament Color on the Dimensional Accuracy and the Tensile Strength of FDM-Printed PLA Specimens," *Polymers*, **15**(10), p. 2377. <https://doi.org/10.3390/polym15102377>.
- [15] Lab, B., 2025, "Introduction to Line Width," Bambu Lab Wiki. [Online]. Available: <https://wiki.bambulab.com/en/software/bambu-studio/parameter/line-width>. [Accessed: 19-Jun-2025].
- [16] "ASTM D638-10 - Standard Test Method for Tensile Properties of Plastics," ITeh Stand. [Online]. Available: <https://standards.iteh.ai/catalog/standards/astm/cbed50c2-95ec-4aa9-80cb-8f7f1f09d460/astm-d638-10>. [Accessed: 20-Jun-2025].